

The ESS HEBT Lattice Design after the 2013 Accelerator Revision

H.D. Thomsen*, S.P. Møller, ISA, Aarhus University, 8000 Aarhus C, Denmark

INTRODUCTION

The year 2013 has brought many changes to the ESS accelerator, even top level beam parameters, while maintaining the average beam power of 5 MW. Indirectly due to the increase in beam current (to compensate for the reduction in beam energy), the concept for expanding the beam on the target surface (the beam entrance window, BEW) has been revisited and changed. Although many requirements remain similar, the changes have required an overhaul of the beam optics of the ESS High Energy Beam Transport (HEBT). Following many iterations stimulated by input from interfacing groups, this report will describe what is expected to be the final magnet layout of the ESS HEBT with optics that are believed to go through only minor future tuning modifications. The present report constitutes the “WP06 delivery A32260” to the ESS.

BEAM OPTICS

The primary line in the HEBT brings the beam from the accelerator to the target, while leaving room for accelerator upgrades, overcoming an 4.5 m elevation, and setting the transverse profiles on the target. These requirements are met through three separate sections with appropriate matching flexibility in between. When the linac is operated in low-power modes, the beam can also be sent to the destination of the dump line, allowing for machine studies and tuning. Space for an additional line, exploiting the high-intensity linac for experiments not related to neutrons, should also be possible but may use up some of the space otherwise intended for energy upgrades of the linac.

A mechanical layout of the final part of the HEBT can be seen in Fig. 1. The purpose and optics of the principal sections will be discussed in the following.

Upgrade High- β (UHB)

As a result of the 2013 design optimization of the linac, the period length along the High- β (HB) elliptical cavity section has been set to 8520 mm of which the cryomodule takes up 6587.6 mm. To allow for future installation of extra cryomodules with HB cavities—thus extending the HB linac—the first part of the HEBT follows the same mechanical layout, albeit at the outset only offering transverse focusing through elliptical linac warm units (EWUs). The layout provides 21 periods for upgrades and contingency, allowing to double the length of the HB linac. In Fig. 2, the 10-RMS beam sizes along the UHB are shown. The

Table 1: Assumed HEBT input beam Twiss parameters.

| | Unit | $w = x$ | $w = y$ | $w = z$ |
|------------------|-----------------|---------|---------|---------|
| α_w | — | -1.728 | 0.165 | 0.153 |
| β_w | mm/ π .mrad | 55.08 | 41.11 | 54.51 |
| $\epsilon_{n,w}$ | π .mm.mrad | 0.344 | 0.359 | 0.395 |

beam sizes can be compared with the foreseen vacuum pipe bore radius of 50 mm along this section. The beam is thus anticipated to be efficiently transported, *i.e.* with very low relative beam losses.

Each EWU’s quadrupole doublet are in the optics powered in pairs by a single power supply, except for the two first EWUs of the HEBT. These four quadrupoles are in the model individually powered and used for matching the linac beam to the UHB transport section. As seen in Fig. 2, the scheme can provide smooth UHB optics (and phase advances), while the beam starts to slightly debunch longitudinally. The gradients of the matching EWUs are about 25% larger than for the rest of the UHB quadrupoles, but still well below the values along the HB, which uses the same magnetic design. Similar matching performance could be obtained by instead using the first four EWUs of the HEBT for matching, most likely leading to lower gradients. The calculated Twiss parameters at the entrance of the HEBT are listed in Tab. 1¹.

The UHB is planned to contain a movable aperture collimator system consisting of 3 collimator stations, ideally located with a transverse phase advance of 60 degrees apart. Due to a slightly lower phase advance in the final optics, the collimator stations—each having 4 jaws—are then foreseen to be located in the long drifts of period 2, 5, and 8.

Achromat

Following the periodic UHB, three quadrupoles match the beam into the vertical achromat, cf. the 10-RMS beam optics shown in Fig. 3. From the perspective of designing the vertically bending magnetic dipoles, it is advantageous to not choose an excessive gap (opening in the horizontal direction), as it considerably affects the magnet size and cost. As seen in Fig. 3, the horizontal beam size can be kept quite small, 10 RMS size $\lesssim 13$ mm. For comparison, the rectangular dipole chamber is expected to be 25×50 mm² ($H \times V$, radius), meaning a minimum aperture of about 20 RMS. Between the pairs of dipoles, three quadrupoles provide the necessary vertical phase advance of 360 degrees,

*heinetho@phys.au.dk

¹Private communications with Mohammad Eshraqi, ESS.

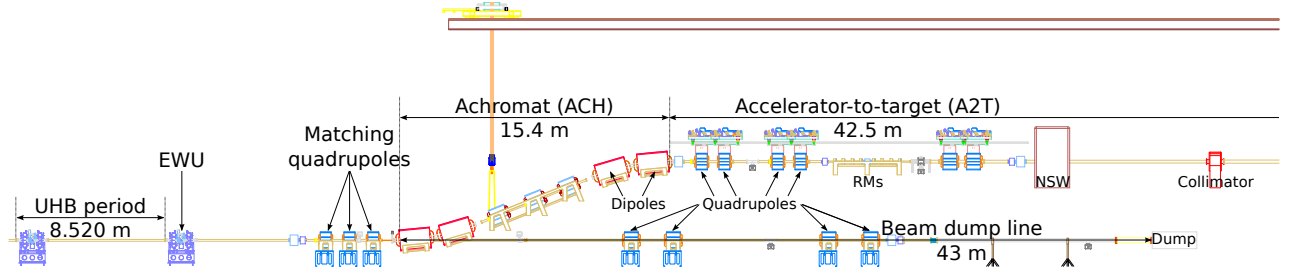


Figure 1: An engineering perspective of the layout of the ESS HEBT (courtesy of Mikael Andersson, ESS). Only the final 2 of the 21 UHB periods are shown to allow for a more detailed view of the remaining part. The individual elements and acronyms will be explained in the following text. An overhead crane is shown and allows for replacement of the ACH and A2T magnets.

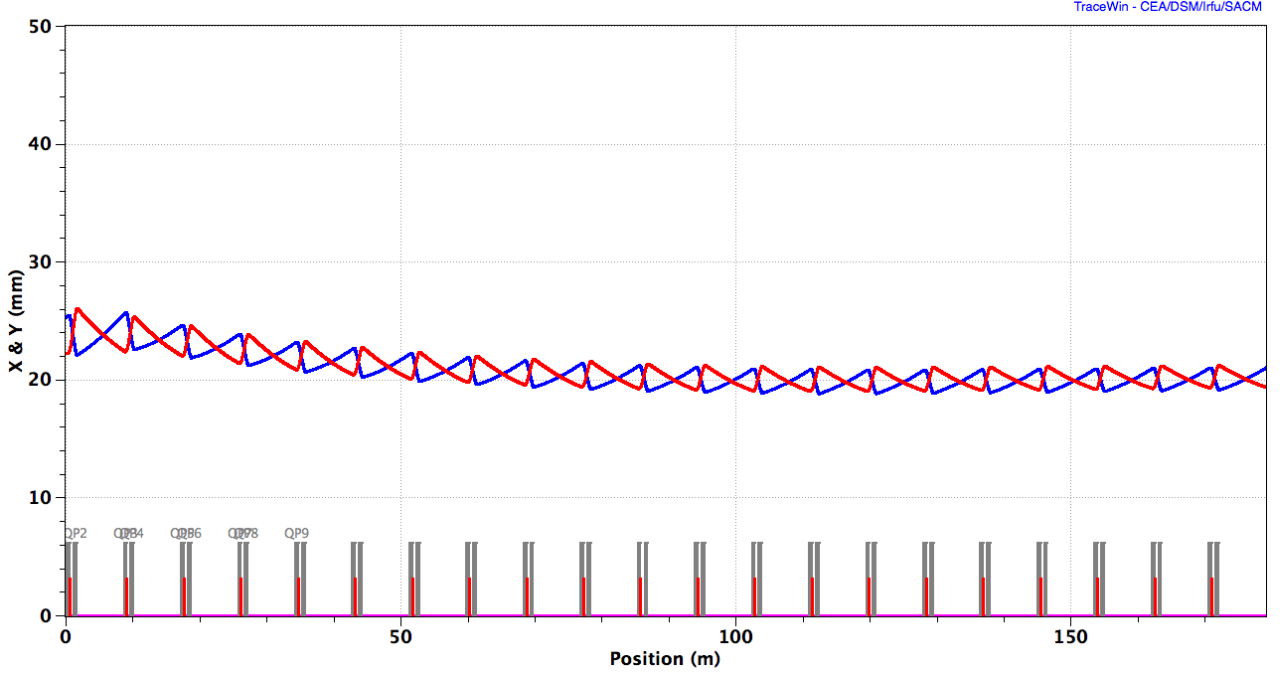


Figure 2: The 10-RMS transverse optics of the UHB. Blue (red) line represents the horizontal (vertical) plane.

thus cancelling the vertical dispersion to first order.

As a result of RF failures along the linac, which may occur on an ultra-fast timescale ($\simeq \mu\text{s}$), the beam may reach the HEBT with a reduced energy, $2.0 \text{ GeV} + \Delta E$. Leaving no time to readjust the downstream magnets, the beam size will be slightly affected and especially the vertical displacement in the dispersive sections will no longer be zero. Here, vertical beam centroid displacements of $\Delta y = (1 + 1/\gamma)^{-1} D_y \Delta E / E \lesssim 0.5 \text{ mm/MeV}$ ($E = 2.0 \text{ GeV}$ assumed) will be introduced. In Fig. 4 the response of the vertical optics following $\Delta E = -30 \text{ MeV}$ can be seen. Notice how the beam centroid (pink line, top panel) becomes non-zero along the achromat and that the dispersion is only approximately cancelled (first order achromat only). In Fig. 5, the uncompensated impact of $\Delta E \neq 0$ on the beam displacement and size on the target's beam entrance window (BEW) can be seen. Since the dominant dispersive contribution is quadratic, non-nominal beam energy

will lead to $\Delta y > 0$ on the BEW. Since only sudden *decreases* of beam energy is expected, its correlation with an increasing beam size is a welcomed feature of the optics, cf. right panel of Fig. 5. At $\Delta E = 50 \text{ MeV}$, the maximum displacement in the achromat is about 25 mm, effectively reducing the 50 mm aperture radius by a factor 2.

Accelerator to Target (A2T)

As described in [1, 2] the idea of using non-linear magnets to deliver more flat beam profiles to the target [3] has during 2013 been abandoned due to its sensitivity towards the characteristics of the incoming beam, in particular the transverse kurtosis, *i.e.* halo. Instead, a linear raster system has been designed which adopts ideas from similar systems designed for the LANL APT [4] and MTS [5].

To introduce oscillating beamlet deflections at the target surface, 8 dithering raster magnet dipoles (RMs), 4 acting in each plane, are foreseen in the A2T. The magnetic field

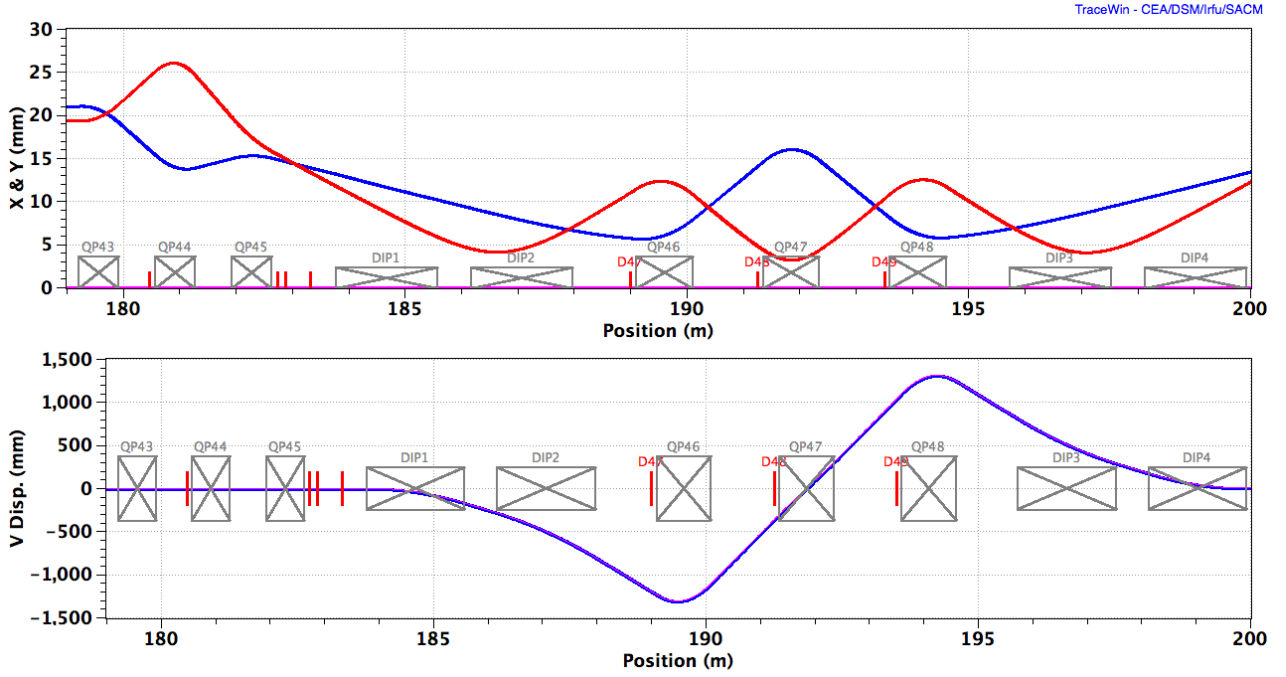


Figure 3: The 10-RMS transverse optics of the achromat and the preceding matching section. Blue (red) line represents the horizontal (vertical) plane. The bottom panel shows the vertical dispersion function, D_y .

of the RMs ideally follow current waveforms of frequencies f_x, f_y

$$f_w = n_w / \Delta t \quad w = x, y, \quad (1)$$

where $\Delta t = 2.86$ ms is the proton pulse duration. For the beamlet to map out the 160×60 mm² rectangular nominal footprint and achieve good intensity uniformity, a linear Lissajous pattern is exploited. The raster pattern is here dictated by the ratio of the sweep frequencies, f_y/f_x , and the waveform shape and relative phase. If n_x and n_y are integers, the beam will be swept in a closed Lissajous-like pattern within one proton pulse. If the integers are additionally chosen as appropriate prime numbers, the rational feature of the ratio is minimized, thus avoiding beat patterns. Examples of integers could be $n_x = 83$ and $n_y = 113$, corresponding to $f_x = 29$ kHz and $f_y = 40$ kHz. Excessive turning times near the raster waveform amplitudes a_w can introduce intensity ridges that are particularly pronounced when the relative beamlet size $\text{RMS}(w)/a_w$ is small. Choosing triangle waveforms minimizes the risk of such burn-ins and increases the uniformity of the accumulated distribution. Fig. 6a shows a pattern corresponding to the mentioned ratio of frequencies and triangle waveforms. The fine-meshed pattern will ensure an good intensity homogeneity within a central rectangle.

The optics of the A2T at nominal RM deflection amplitude in both planes can be seen in Fig. 7. A common dipole action point (AP), the apparent origin of the deflection in both planes, is obtained by placing the 4 + 4 RMs with mirror symmetry, $B_y B_y B_x B_x (AP) B_x B_x B_y B_y$. The RMs are expected to be mechanically identical: a 200 mm long

window frame ferrite yoke with thin, saddle-shaped copper plate coils. To limit eddy currents, a ceramic vacuum chamber is foreseen, possibly with its inner surface being metalized (few micron of titanium) to conduct the beam image currents. The vacuum pipe inner aperture is modelled as $\varnothing 80$ mm, whereas the magnetic design assumes a yoke aperture of 100×100 mm. Downstream of the RMs a quadrupole doublet, Q5+Q6, not only ensures the final beam size expansion, but their strengths are constrained to impose a transverse phase advance of π between the AP and the beam crossover (CO). The centroid displacements introduced by the RMs are hence neutralized by design at the CO, which becomes a pivot point for the oscillating deflections. This transport line concept is inspired by the MTS line [5]. The CO doublet, Q5+Q6, is arranged such that its angular magnification compensates for the $\simeq 4:1$ aspect ratio of the pattern amplitudes, thus balancing the necessary RM peak fields in the two planes. In the presented optics, the peak integrated field per RM is $\int B_y dL = 2.4$ mT.m or $\int B_x dL = 3.3$ mT.m.

Apart from setting the beamlet size on the target, the upstream matching quads, Q1–Q4, provide a beam waist at the CO, where the beam deflections are minimized by design. The CO is thus a suitable location for a small-aperture shield that limits the intensity of back-streaming neutrons during operation. In Fig. 7, a neutron shield wall (NSW) with a $\varnothing 40$ mm \times 2000 mm aperture is shown centered around the CO beam waist. Not shown in the figure are four separate 2D dipole correctors which will help correct the transverse beam displacement and angle before going through the RM and CO apertures. This correction proce-

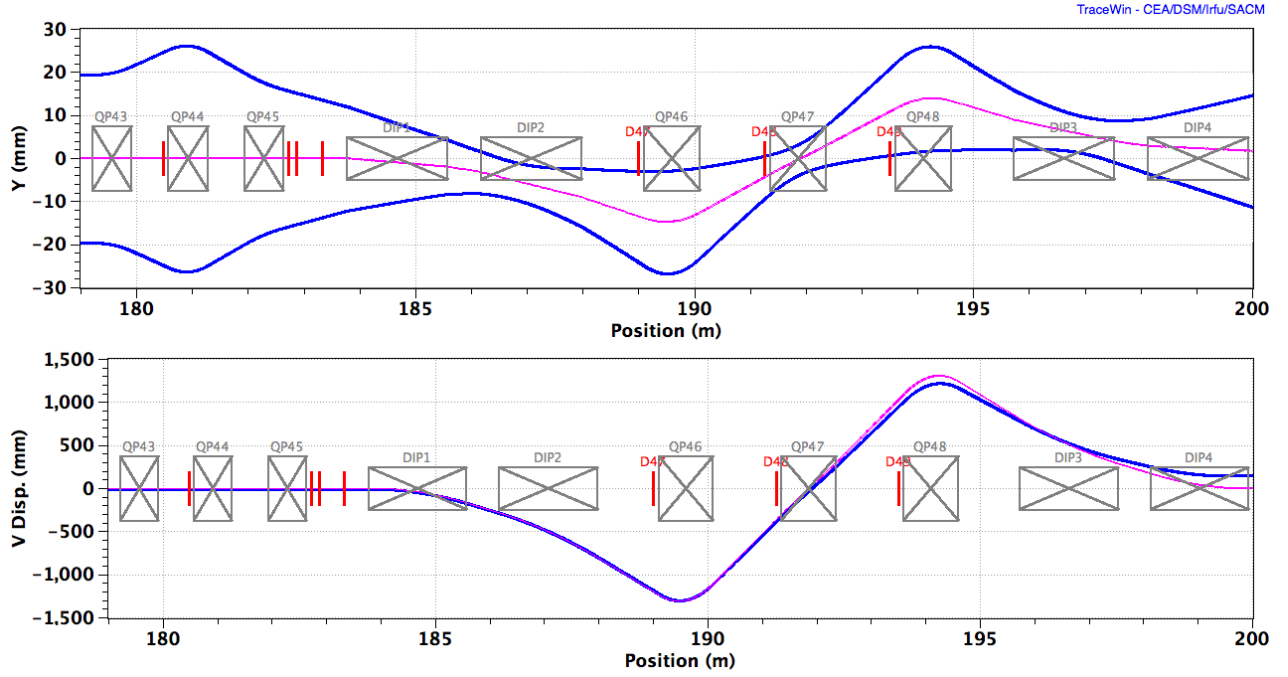


Figure 4: The 10-RMS vertical optics of the achromat in the case of $\Delta E = -30$ MeV. In the bottom panel, the pink line represents the linear dispersion, whereas the blue line represents higher order dispersion.

ture can advantageously be performed with a low-power (short-pulse) accelerator mode, while having the RMs off. One of the pairs of DC correctors is placed with mirror symmetry around the AP. Turning off the RMs, these can thus be used to verify the displacement neutralization at the CO and angular magnification of Q5–Q6 while avoiding the complexity of the AC raster motion. Such constant displacements on the PBW and BEW will be necessary for calibrating luminescent coatings applied in target imaging systems.

Using TraceWin [6] including 3D space charge, the line's transport of 5×10^6 multiparticles indicates a minimum waist RMS size of $\lesssim 0.4$ mm at the CO. The beam parameters at other locations can be inspected in Tab. 2. Assuming these parameters and a 2D Gaussian beamlet distribution, the intensity distribution at the BEW has been simulated by generating a total of 2×10^9 multiparticles. The distribution is scaled to represent the peak current density normalized to the average beam current of 2.5 mA, cf. Fig. 6b. Overall the distribution is very smooth containing no undesirable artifacts generated by the expander system. Within the central 100×10 mm², the uniformity has been found to be better than 1.5%. This is an impressive result, considering the low complexity of generating and verifying the pattern. The assumption of a pure Gaussian beamlet may seem crude, but more complex distributions (including a description of transverse halo) have been implemented in the simulations, leading to hardly noticeable changes to the accumulated distribution.

Fig. 8 shows a comparison between the linear optics model and a multiparticle simulation, both calculated us-

ing TraceWin. The latter assumes 5×10^6 multiparticles following Gaussian phase space distributions. A 1% artificial Gaussian with 5 times nominal emittance is added to all three phase spaces to represent halo particles. The combined distribution has been transported through the entire HEBT, and the comparison only shows the final 45 m before the target. In general, the linear model optics appears to describe the simulation results very well, even to the relative level of 10^{-6} , and the beam is transported through the line and CO aperture without observing any losses in the simulations, contrary to the previously foreseen application of non-linear magnets. Although successful in generating semi-uniform profiles at the target, the non-linear system's unintentional aberrations and strong sensitivity towards the transverse beam halo were highly undesirable. The raster system's apparent compliance with a linear model could signify simple operation of the future line. Due to the limited magnification of the linac beamlet and the raster pattern's smearing of the beamlet, the transverse halo has a limited effect on the accumulated beam profile at the target.

Beam Losses

As a first approach to evaluate the beam losses in the HEBT, the vacuum pipe bore radius (with RM centroid deflection subtracted, where relevant) has been calculated in units of the local beam RMS sizes along the HEBT. This normalized aperture is calculated in each transverse plane and shown in Fig. 9. The normalized aperture generally stays above 20, except for the final 20 m drift between the CO and target. It should be noted that the physical aper-

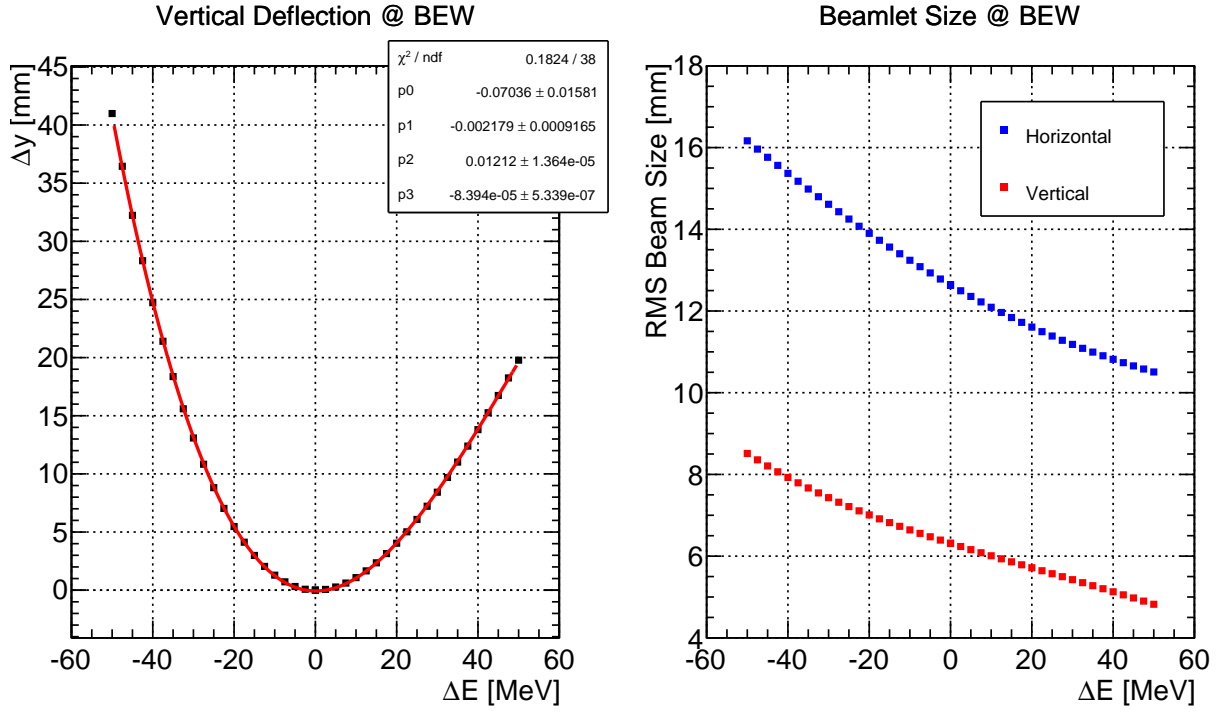


Figure 5: The beam's vertical displacement and beam size on the BEW as a function of ΔE .

Table 2: Beam parameters, horizontal (H) and vertical (V).

| Parameter | Location | H | V |
|----------------------|----------|------------------------------|---------|
| RMS size | CO | 0.2 mm | 0.4 mm |
| | PBW | 10.0 mm | 5.00 mm |
| | BEW | 12.6 mm | 6.32 mm |
| Max. deflection | PBW | 55.4 mm | 12.7 mm |
| | BEW | 70.0 mm | 16.0 mm |
| Avg. current density | PBW | $88 \mu\text{A}/\text{cm}^2$ | |
| | BEW | $56 \mu\text{A}/\text{cm}^2$ | |

tures in this section are still under discussion. By comparing the two panels of Fig. 9 showing the normalized aperture at maximum (top panel) and zero RM field (bottom panel), it is seen that especially the horizontal deflection here has a considerable impact on the calculated quantity. For reference, the normalized aperture in the SNS cold linac is $\simeq 10$ [7], hence the uncontrolled beam losses along the ESS HEBT are in general expected to be low.

Beam Dump Line (DMPL)

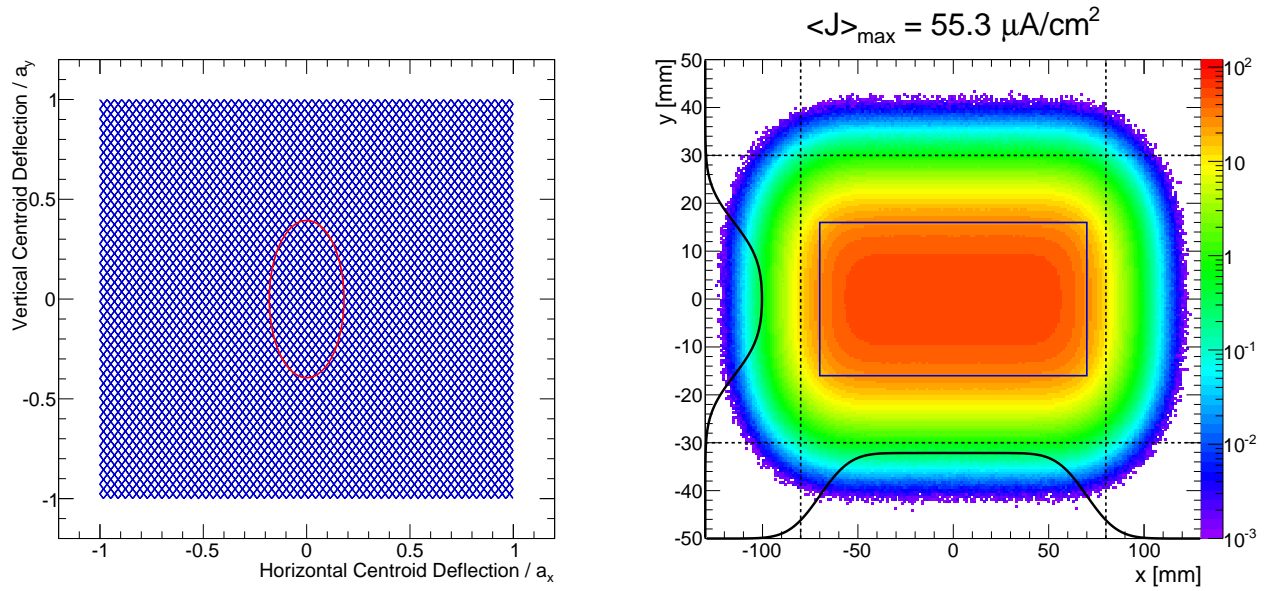
With the dipoles of the achromat set at zero field, the beam will be sent to a tuning dump in line of sight with the linac. The beam dump is specified for 50 kW beam power (2.0 GeV, 1 Hz, $\Delta t = 0.4$ ms). With the lower beam power, this destination allows for larger relative beam losses while still respecting the requirements for hands-on maintenance. Slightly lower normalized apertures should thus be ac-

ceptable in the HEBT dump line (DMPL). The 10-RMS optics can be seen in Fig. 10. The achromat matching quadrupoles—visible far upstream in the figure—are left at their nominal gradients, leaving the absent dipole field as the first difference from the nominal, full-power optics. The DMPL contains a 2×2 quadrupole matching section which introduces a beam waist (at the D48 marker in Fig. 10) and sets the nominal RMS size of 12.5 mm (in both transverse directions) at the beam dump surface. In the center of each quadrupole doublet, a 2D dipole corrector is located to center the beam relative to the dump. The normalized aperture is seen to stay above at least 10 throughout the DMPL.

CONCLUSION

The optics of the ESS HEBT following a major revision has been presented. In general, the HEBT line can efficiently bring the beam from the linac to the target. Each of the principal HEBT sections (UHB, achromat, A2T) also provides separate matching sections to control the transverse beam parameters, thus offering tuning flexibility towards deviations from nominal beam parameters.

The transport line's sensitivity towards dynamic errors has yet only been tentatively studied, which has revealed a non-negligible sensitivity towards changes in the beam energy. This is to be studied further using multiparticle studies including longitudinal halo, allowing to assess likely loss patterns in the achromat. Additional planned studies include error and alignment studies. Comparing the optics with the current assumptions on the vacuum apertures, the



(a) A Lissajous-pattern generated by triangle waveforms with a frequency ratio of 113/83. For comparison, the beamlet relative RMS sizes at the BEW are illustrated by a red ellipse.

(b) The intensity distribution is scaled to represent the peak current density, normalized to 2.5 mA average current. The blue rectangle illustrates the outline of the raster pattern.

Figure 6: Simulated raster pattern and consequent intensity distribution at the target BEW, following a full cycle of the Lissajous-pattern with the beam parameters in Tab. 2.

uncontrollable beam losses are expected to be low, as the normalized aperture is comparable or better than at similar facilities, like the SNS. Additionally, all electron detachment loss mechanisms involved with H^- beams will not be present in the ESS proton accelerator.

REFERENCES

- [1] H.D. Thomsen *et al.*, IPAC'13, MOPEA005, p. 70 (2013).
- [2] T.J. Shea *et al.*, NA-PAC'13, MOPMA04 (2013).
- [3] A.I.S. Holm *et al.*, IPAC'12, MOPPD049, p. 475 (2012).
- [4] S. Chapelle *et al.*, LINAC'98, TU4089, p. 612 (1998).
- [5] B. Blind *et al.*, LINAC 2006, MOP055, p. 171 (2006).
- [6] R. Duperrier *et al.*, ICCS'02, LNCS2331, p. 411 (2002).
- [7] A. Shishlo *et al.*, IPAC'12, TUOBA03 (2012).

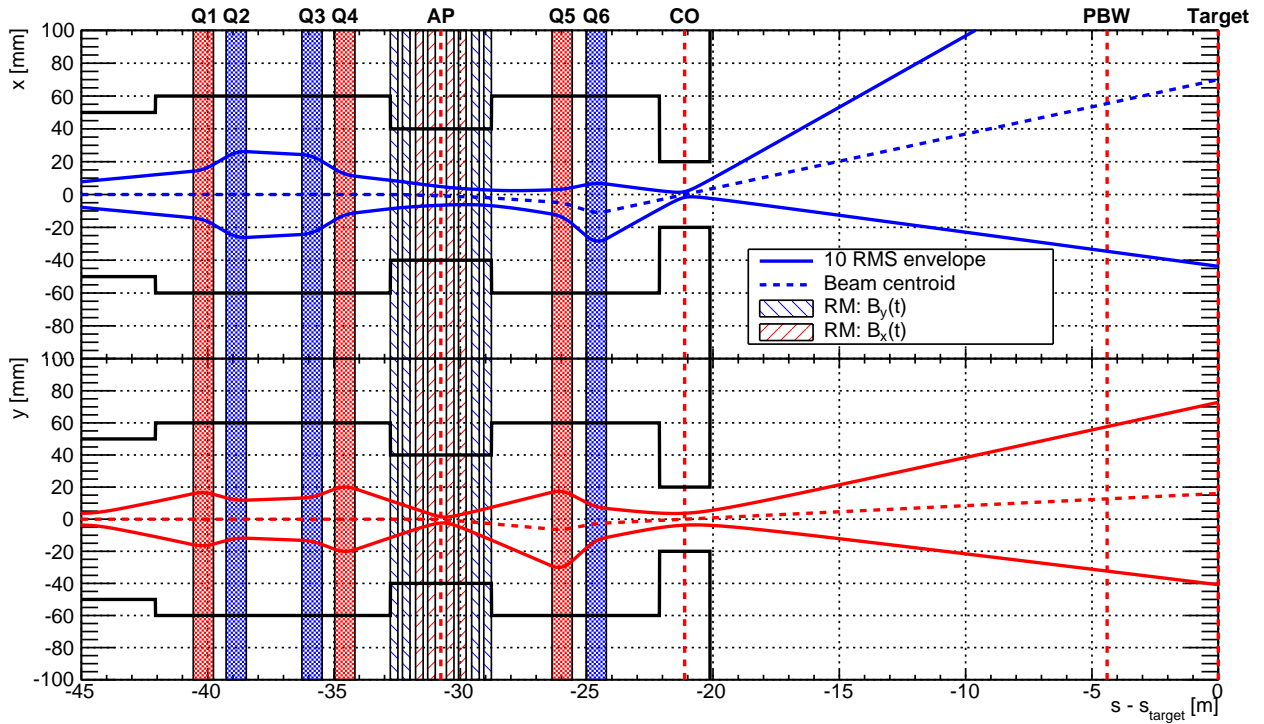


Figure 7: The final 45 m of the HEBT before the target surface. The optics is shown at nominal RM deflection amplitude.

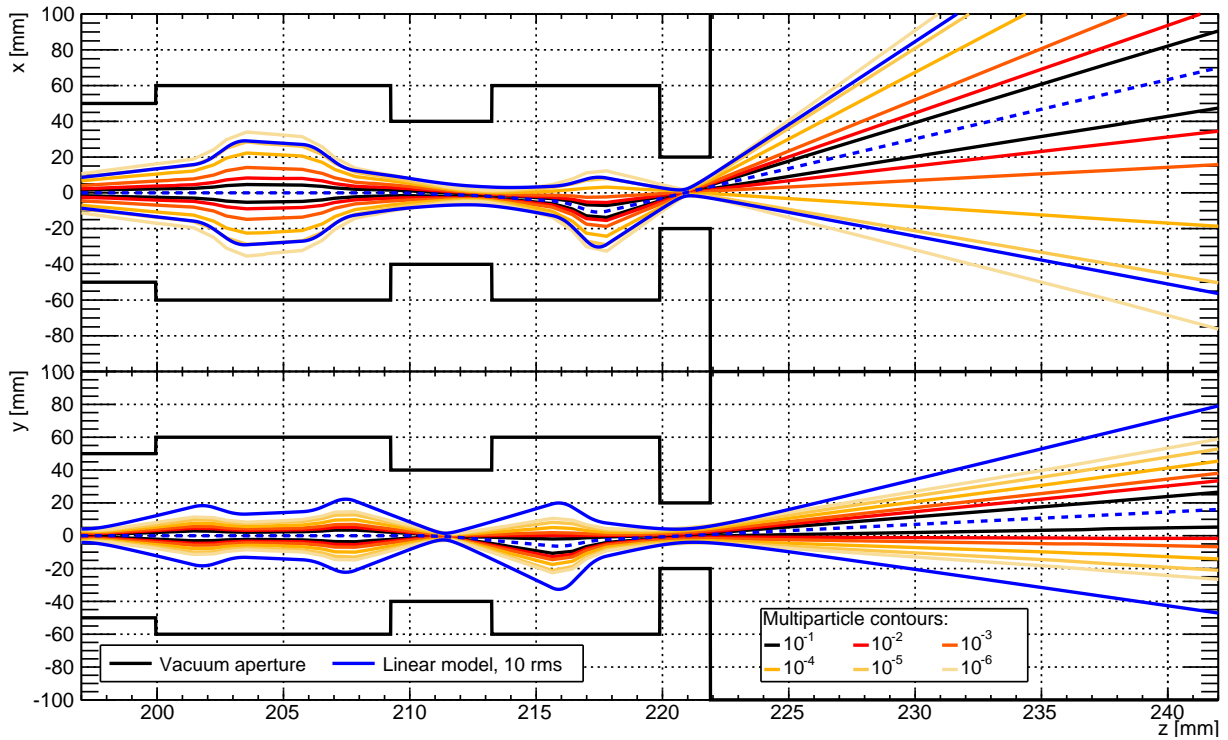
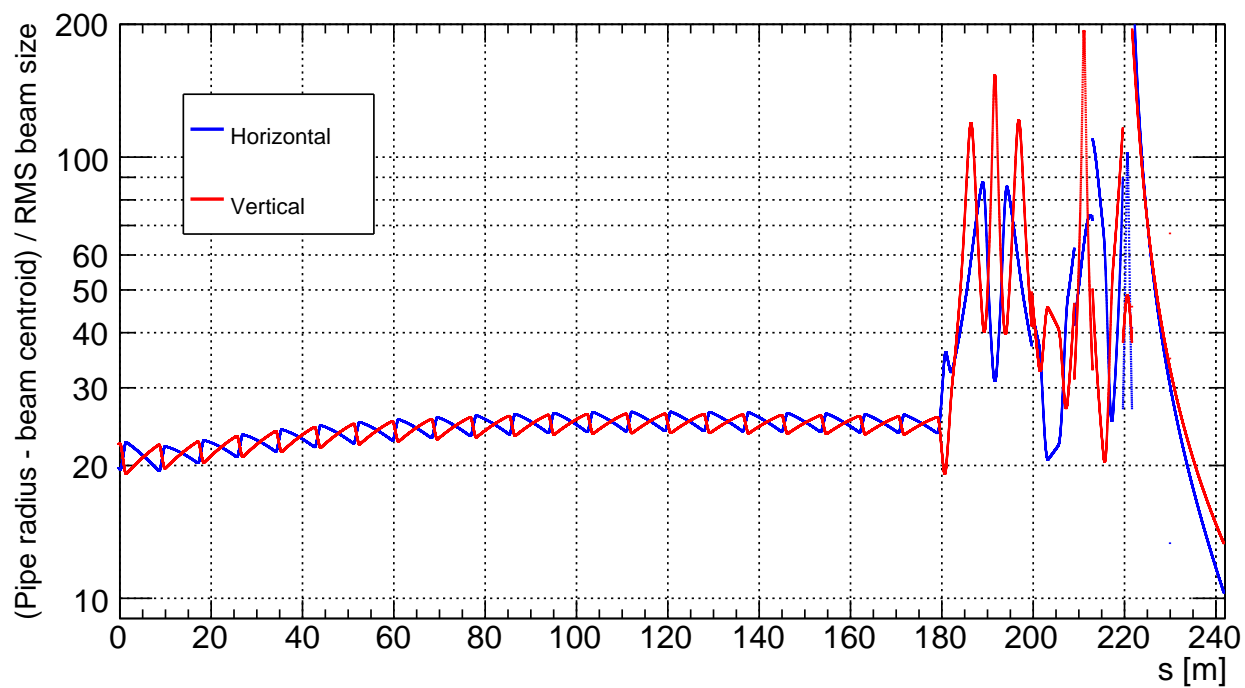
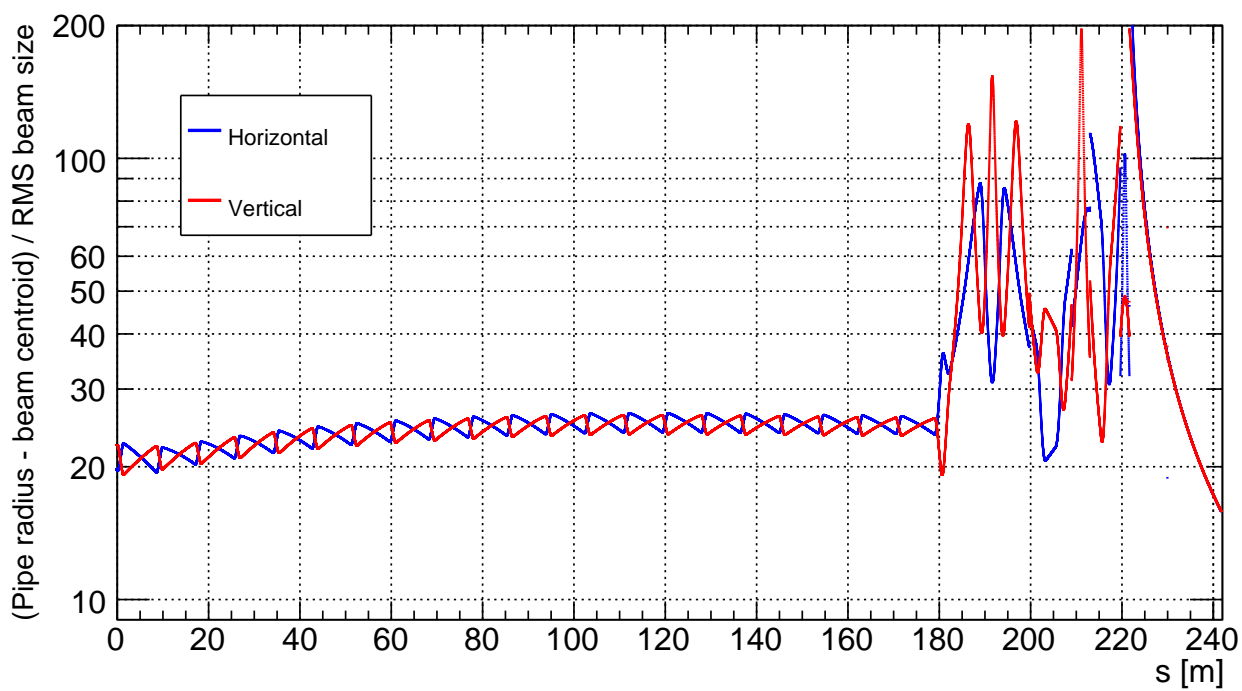


Figure 8: A comparison between a multiparticle simulation and the corresponding transverse linear optics.



(a) RMs at maximum nominal field.



(b) RMs at zero field.

Figure 9: The minimum distance from beam centroid to vacuum pipe inner surface in units of beam size RMS. The values are calculated including the RM deflection, where relevant. The calculated ratio follows the jump discontinuities contained in the aperture model.

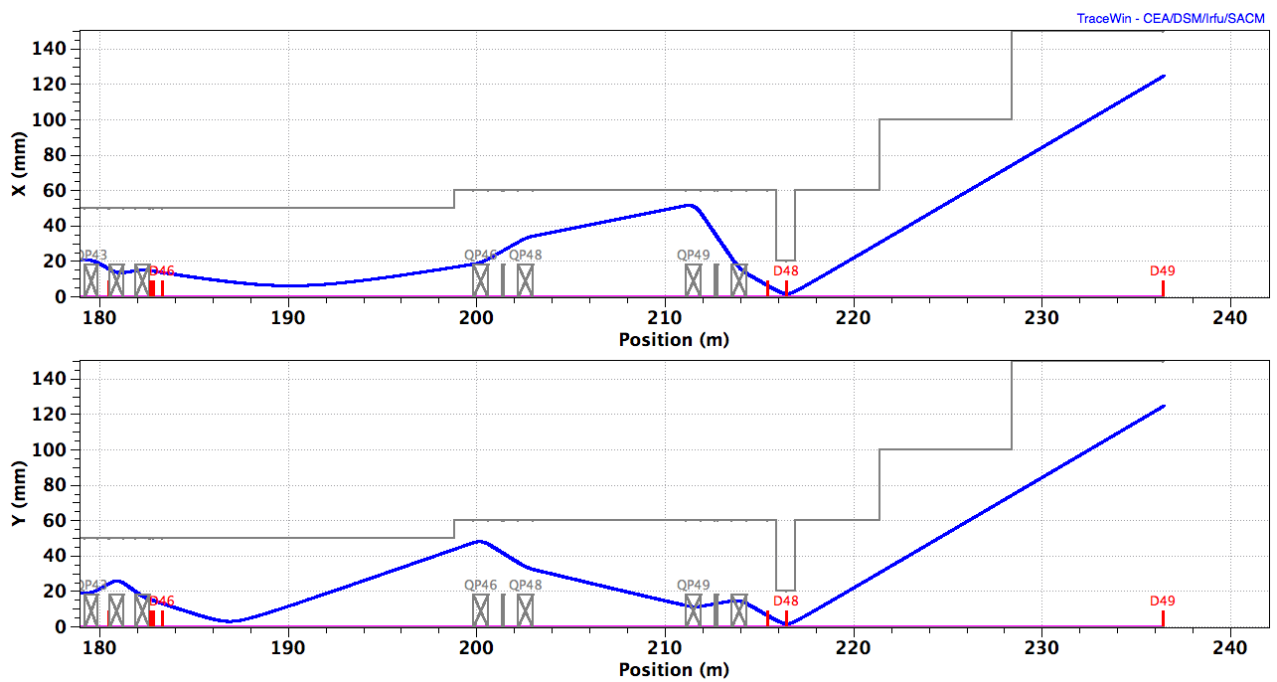


Figure 10: The 10-RMS transverse optics of the beam dump line with the dump located at the far right at marker D49.